Beam Performance

Developments and Upgrades of Storage Ring

Improvement of Current Stability in Top-up Operation

The top-up operation of the SPring-8 storage ring started in September 2004 with the purpose of improving the average brilliance and stabilizing the stored current and the source intensity. Since the beginning of the top-up operation a stability of the stored current of 0.1% (100 μA) has been achieved. For example, Fig. 1 shows a typical trend of the stored current in October 2007. This high regularity of the stored current is profitable for user experiments, particularly for those requiring precision [1,2].

In the top-up operation of SPring-8 the injected current per shot is fixed to 30 μA to maintain the uniformity of the bunch currents of the several-bunch filling mode. In contrast, due to user requirements, the interval between the beam injections is fixed to 1 minute for the several-bunch filling mode and 5 minutes for the multi-bunch filling mode. Hence, the injected current of 30 μA does not compensate the decrease in stored current, and the shot number at each beam injection is unsettled and varies from 1 to 3. Thus, the deviation of the stored current becomes 0.1% (100 μA), although the injected beam current is 30 μA. Since the stored beam oscillation at injection is now well suppressed by machine tuning [3-5], users do not need to know the timing of the beam injection. In November 2007 we hence decided to reduce the interval between beam injections to improve the stored current stability.

In the new top-up mode the interval between beam injections is variable so that just one shot is injected at each injection. We call the new top-up operation the current prior mode and the old operation the interval prior mode. Figure 2 shows the trend of the stored beam current in the new mode. The deviation of the stored current is 30 μA, which corresponds to the injected current, as expected. At the time of measurement the beam lifetime was around 18 hours, so the average interval between beam injections was 20 seconds. Figure 3 shows the stored current distributions over 8 hours in both modes, which clearly shows that a current stability of the SPring-8 storage ring of 0.03% is achieved. We expect that this high stability of the stored current will contribute to the improvement of user experiments.

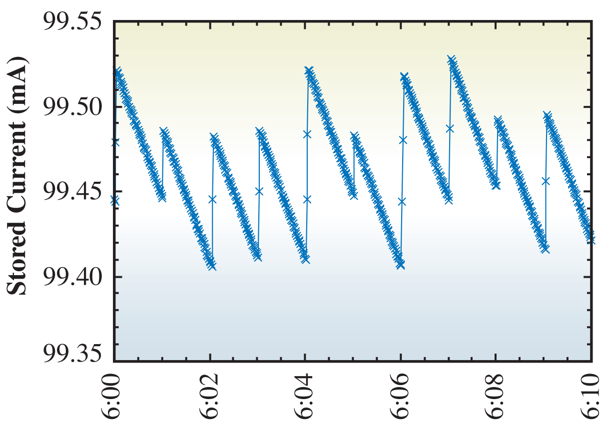

Fig. 1. Trend of the stored current over 10 minutes before the mode change of the top-up operation.

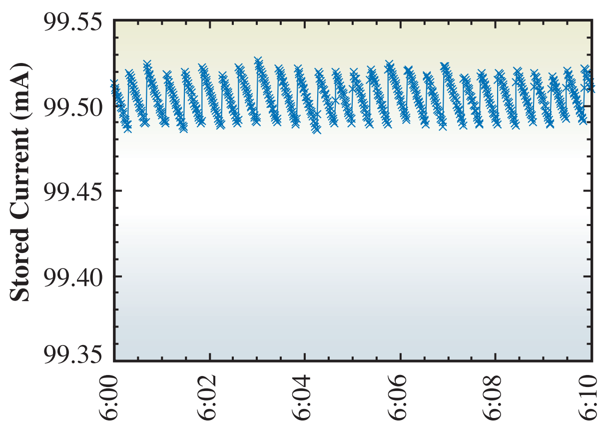

Fig. 2. Trend of the stored current over 10 minutes after the mode change of the top-up operation.

Development of Remote Tilt-Control System for Injection Bump Magnet of the Storage Ring

In the top-up operation mode, it is important to suppress the oscillation of the stored beam at beam injection. To generate a bump orbit, four bump magnets (BP1 - BP4) are excited with pulsed current by four different power supplies. These pulses are synchronized to the timing of the beam injection. The waveform of the excitation current is a half-sinusoidal shape with a pulse width of 8 μsec. If not all the pulses are the same shape, the stored beam is oscillated in the horizontal direction by the bump magnets. Furthermore, if the bump magnets have an alignment error in their rotation around the beam axis (tilt), the stored beam is also oscillated in the vertical direction.

To reduce the oscillation amplitude of the stored beam, we measured the beam oscillation using a turn-by-turn beam position monitor (BPM). By using the measured beam position data of the horizontal oscillation, we can estimate error kicks by the bump magnets and adjust their pulse height and timing. The vertical oscillation can also be reduced by estimating

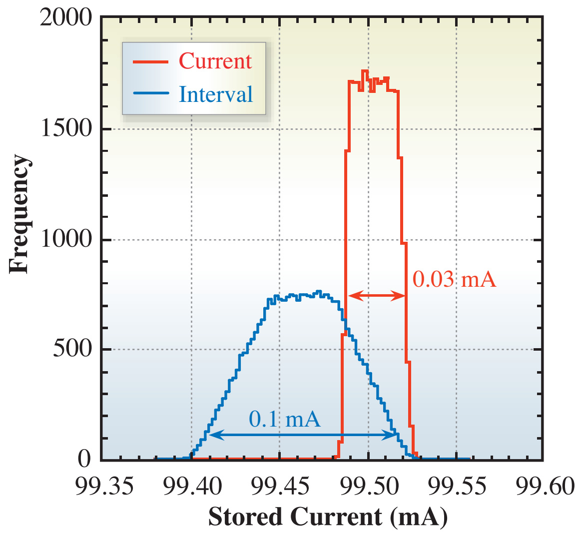

Fig. 3. Distributions of the stored current over 8 hours in both top-up operation modes.

the tilt of the bump magnets with the turn-by-turn beam position data. The process of adjusting the tilt is not easy and the oscillation measurement and tilt adjustment must be repeated two or three times [3]. We then developed a remote tilt-control system to ensure smooth realignment. The power machinery of the system is shown in Fig. 4. A bump magnet is placed on a stainless-steel plate. A stepper motor is attached to one side of the plate through a 1/30 warm gear. The other side of the plate is supported at two fixed points. The bump magnet is tilted in the clockwise direction if the stepper-motor side is moved upward. The range of adjustment is ±4 mrad with a resolution of 8.74 μrad / 1000 pulses.

The system was initially installed for one bump magnet (BP4). To confirm the response of the system, the tilt and rotation around the x-axis (pitch) were measured using a leveling instrument placed on top of the bump magnet. The stage was moved clockwise, then counterclockwise and then clockwise (see Fig. 5). As a result, the obtained backlash of the system was 0.827 mrad. The reproducibility was 6.4 μrad when the tilt was increased or decreased monotonically in the same direction. The measured tilt agreed with the set tilt within 5%. The change in the pitch upon controlling the tilt was less than 3%.

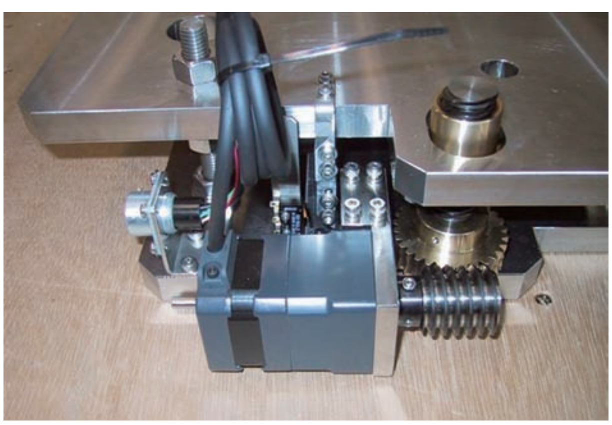

Fig. 4. Power machinery of a remote tilt-control system. A stepper motor (shown in the center of the picture) adjusts the tilt of the stage for a bump magnet. The bump magnet was placed on the stage. The beam travels from right to left in this figure. A rotary encoder was also attached to measure the number of rotations of the motor.

Figure 6 shows the rms amplitude of the measured vertical beam oscillation before and after adjusting the tilt of the bump magnets. The solid black line is the oscillation amplitude before turn-by-turn adjustment using the BPMs. In this measurement, the beam was stored in one RF bucket and the bump magnets were excited without injection. Using this data, we estimated the tilt errors of BP1 and BP4. The tilt of BP1 was adjusted manually on the site and that of BP4 was adjusted using the newly developed remote control system. The result is shown in Fig. 6 by the solid red line. The amplitude was well reduced to the level of resolution of the turn-by-turn BPM system. In the future, we will install the same tilt-control system for BP1 - BP3 for the complete on-beam reduction of the vertical oscillation.

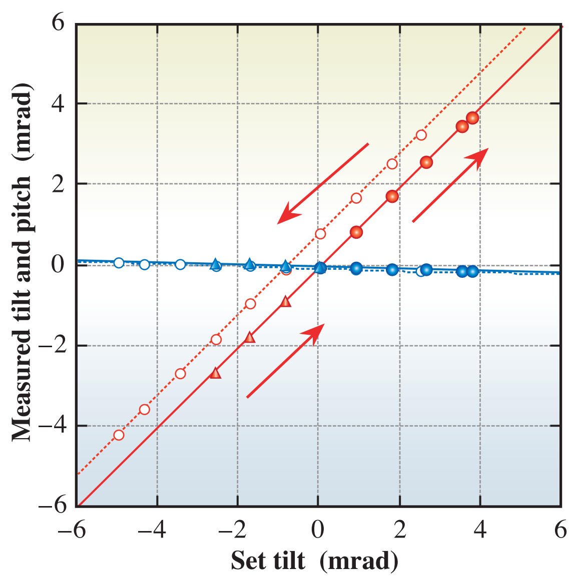

Fig. 5. Measured tilt and pitch of the bump magnet BP4 at various set values of the tilt. Solid red circles and open red circles indicate the measured tilt under clockwise and counterclockwise changes, respectively. Solid red triangles indicate the measured tilt under the subsequent clockwise change. Solid black circles and open black circles indicate the measured pitch under clockwise and counterclockwise changes, respectively.

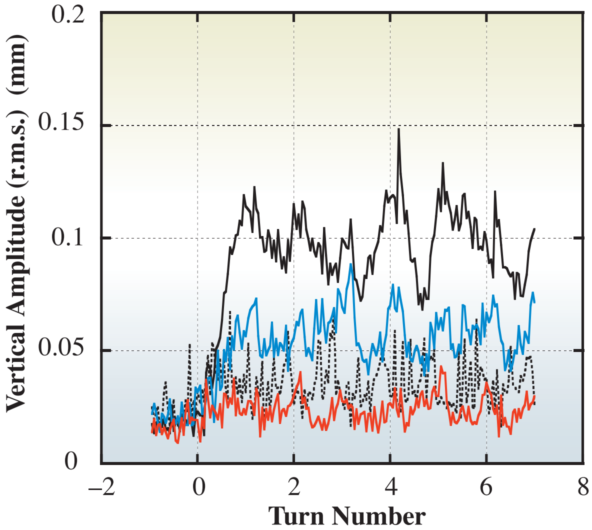

Fig. 6. Amplitude of the vertical oscillation of a stored beam induced by bump magnets. Measured values of r.m.s. amplitude are plotted as a function of the turn number (revolutions of the beam). The solid black, blue and red lines indicate the amplitude before adjustment, after BP4 remote adjustment and after BP1 and BP4 adjustment, respectively. The broken black line indicates the amplitude before installing the remote tilt-control system.

Linear Resonance Coupling Correction

The betatron coupling is one of the most important parameters of storage rings for a high brilliant light source, since it generates the vertical spread of the stored beam and hence reduces the brilliance of the radiated photon beam. By the precise alignment of the magnets [6] and the proper COD correction [7], we have succeeded in achieving very small linear betatron coupling without skew quadrupole corrector magnets since the commissioning phase of the SPring-8 storage ring. As the linear coupling is essential for the light source, we have routinely observed the resonance coupling. The method of observing the resonance coupling is as follows. The operation point of the SPring-8 storage ring is (β_x, β_y) = (40.15, 18.35); thus, the nearest linear resonance $\nu_x - \nu_y = 22$ has the greatest effect on the beam dynamics. The perturbation theory with single resonance approximation implies that the vertical beam size σ_y in the vicinity of the resonance is described as [8]

$$\sigma_y{}^2 = \frac{\frac{1}{2}|C|^2}{|C|^2 + \Delta^2}\beta_y \varepsilon_0 \, , \qquad (1)$$

where C is the coupling driving term, $\Delta(= \nu_x - \nu_y - 22)$ is the distance from the resonance, β_v is the vertical betatron function and ε_0 is the natural emittance. The coupling driving term is given by the integration of the error skew quadrupole magnetic field over the circumference, and reflects the performance of the machine. Hence, the more we reduce the coupling driving term, the smaller we can make the vertical beam size. From Eq. (1), we find that the vertical beam size has a Lorentzian-like variation with the distance from the resonance and that the width of the resonance is given by the strength of the coupling driving term. Figure 7 shows the trend of the measured vertical beam size near the resonance. In Fig. 7, "Ac" means the achromat optics, and "LE" represents the low emittance optics. Before September 2005 the storage ring was operated using the achromat optics with 6.6 nmrad emittance, and since then the low emittance optics with an emittance of 3.4 nmrad. Hence, the peak at the resonance, i.e., the maximum vertical beam size, is reduced after this change in optics.

From Fig. 7 one immediately finds that the coupling strength has grown year after year since 2004. Thus, we decided to correct the resonance coupling to improve the machine performance. Since the resonance coupling possesses two degrees of freedom, we correct it using two sets of skew quadrupole magnets, which have been installed in the SPring-8 storage ring. One set is installed at the arc section of every two normal cells, and the other is installed close to the entry and exit of each long straight section. The phase difference of these two families with respect to the linear resonance is almost 90°, which is favorable for the coupling correction. The coupling correction was carried out near the resonance $\Delta = 0.03$ for easy the observation of the response of the vertical beam size against the change in strength of the skew quadrupole magnets. The process of coupling correction is shown in Fig. 8, where the red

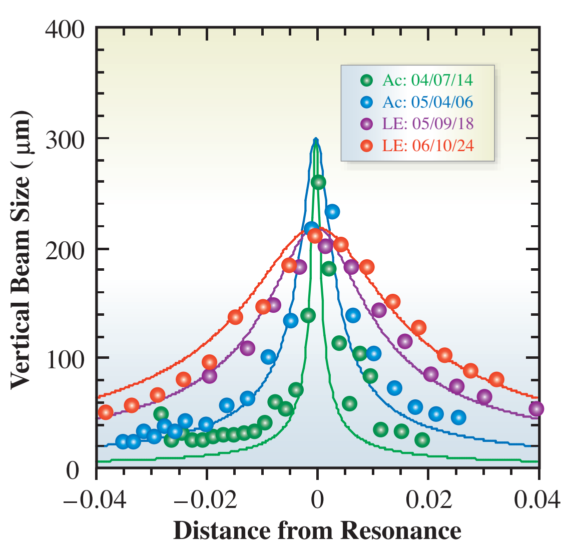

Fig. 7. Trend of the behavior of the vertical beam size in the vicinity of the nearest linear resonance.

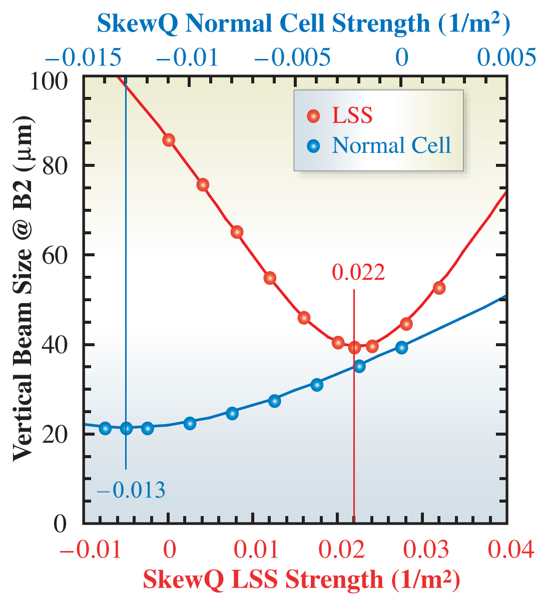

Fig. 8. Correction of the resonance coupling using the skew quadrupole magnet.

circles denote the response to the tuning of the skew quadrupole magnets at the long straight sections and the blue ones denote those at the normal cells. The lower ordinate in Fig. 8 denotes the total strength of the skew quadrupole magnets at the long straight sections and the upper ordinate represents that at the normal cells. By minimizing the vertical beam size, as shown in Fig. 8, we correct the resonance coupling. After the coupling correction, we observe the resonance coupling to confirm the performance of the correction, whose result is shown in Fig. 9. The strengths of the resonance coupling are estimated to be 0.012 and 0.001, respectively, before and after the correction, and thus we can correct the resonance coupling effectively. Although the operation point in user time is sufficiently far from the resonance, i.e., $\Delta = 0.2$, it is observed that the coupling correction improves the vertical beam size by a few percent.

Installation of Counter-Sextupole Magnets in the Storage Ring

In the SPring-8 storage ring there are four magnet-free long straight sections of about 30 m length. These long straight sections were realized in 2000 by locally rearranging quadrupole and sextupole magnets. At that time we maintained the periodicity of the cell structure, especially that of sextupole field distribution along the ring. To keep the periodicity high and hence the dynamic aperture large when modifying the optics, we adopted a scheme in which "betatron phase matching" and "local chromaticity correction" are combined. In this scheme the dynamic aperture for on-momentum electrons is kept by the phase matching and that for off-momentum electrons is enlarged by the local chromaticity correction with weak sextupoles (SFL).

To further improve the symmetry of the ring, we installed "counter-sextupole magnets" in every long straight section in 2007. These magnets are placed 180° apart from SFL in the horizontal betatron phase. The counter-sextupole magnets can minimize the harmful effect of nonlinear kick due to the SFL [9]. After the beam tuning we confirmed that the dynamic aperture and the momentum acceptance were indeed improved.

Figure 10 shows the Touschek beam lifetime measured at the stored current of 1 mA/bunch with and without the counter-sextupole magnets. The Touschek

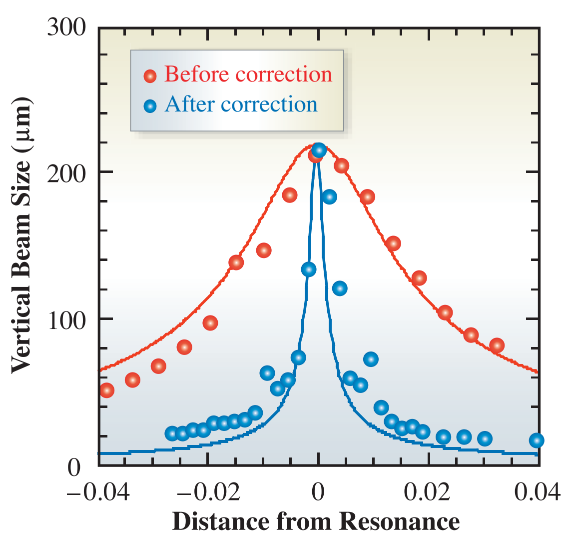

Fig. 9. Vertical beam size in the vicinity of the linear resonance before and after the coupling correction.

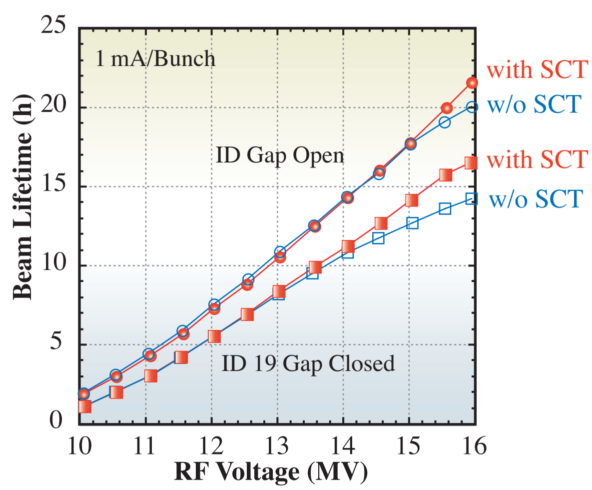

Fig. 10. Touschek beam lifetime at 1 mA/bunch as a function of RF accelerating voltage measured in the optics with and without the counter-sextupole magnets (SCT).

beam lifetime is an index of the momentum acceptance, and a longer beam lifetime at high RF accelerating voltages means larger momentum acceptance. From the figure we see that when the counter-sextupole magnets are used, the beam lifetime becomes longer at high RF voltages and hence the momentum acceptance becomes larger. This tendency in the Touschek beam lifetime can be seen more clearly when the gap of the 25-m-long in-vacuum undulator is closed, as also shown in the figure.

In Fig. 11 we plot the injection efficiency as a function of the horizontal position of an injected beam at the end of a beam transport line from the booster. The injection efficiency is higher when the counter-sextupole magnets are used. This means that the storage ring has a larger dynamic aperture, and beam loss during injection is reduced.

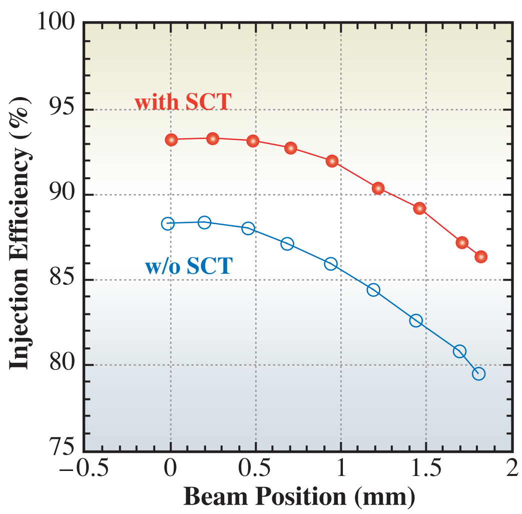

Fig. 11. Injection efficiency as a function of the horizontal position of an injected beam at the end of a beam transport line. The origin of the abscissa is the nominal beam position and a positive value corresponds to a position further away from the stored beam orbit.

Elimination of the Filling Pattern Dependence of the BPM Signal Processing Circuits

The signal processing electronics of the storage ring beam position monitors (BPMs) were replaced during the summer shutdown of 2006, as reported in Research Frontiers 2006 [10]. As a result, the speed and resolution of the closed-orbit distortion (COD) measurements improved. However, the differences of the COD data between different filling patterns reached over 100 μm, although the actual orbits were expected to be the same.

Some typical filling patterns of the SPring-8 storage ring are listed in Table 1. From the list, it is shown that current in a bunch varies by more than two orders of magnitude, and hence the voltage signal amplitude at the circuit inputs can change by the same amount according to the change of the filling pattern.

However, the intensity of the RF acceleration frequency component and its harmonics in the beam signal spectrum are independent of the filling pattern; the RF harmonics depend on the stored beam current and the shape of bunch pulse. The change of the filling pattern varies the intensities of the revolution frequency harmonics except for the RF harmonics. This intensity variation contributes to the large change of the voltage signal amplitude. To avoid the influence of the change of the filling pattern, we arranged the signal processing circuits of the BPM so that only the RF acceleration frequency component in the beam signal was detected.

Nevertheless, large differences of COD data with the change of the filling patterns resulted. The cause of the differences was attributed to the nonlinear response of the diodes used for protecting the multiplexers from electrostatic discharges. The filter-switch module, which is in the front part of the circuits, contains the low-pass filters, the RF switch and the diodes to protect the switch IC from excessive voltages, as shown in Fig. 12. This part is upstream of the place where the RF frequency component is selected; hence, the change of the filling pattern induces the large variation of the voltage signal amplitude at the diodes. When a large voltage signal was input to the circuit, the protective diodes were partially conductive, which resulted in the nonlinear response of the circuits. This nonlinearity induced by the diodes caused the filling pattern dependence.

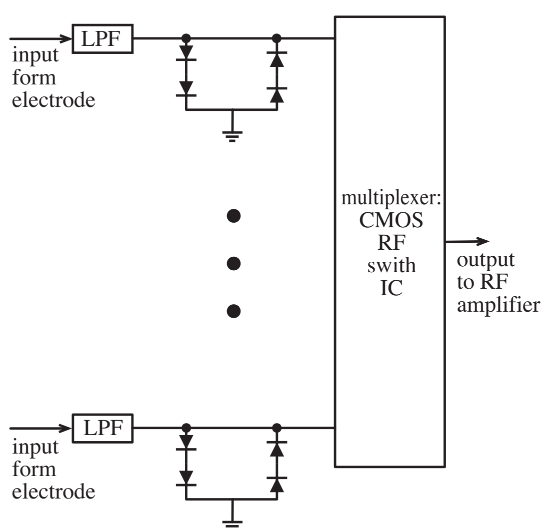

Fig. 12. Schematic diagram of the filter-switch module that is composed of the low pass filters (LPF) with 700 MHz cutoff frequency, CMOS RF switch IC and the diodes between them to protect the switch IC from excessive voltages.

Table 1. Examples of typical filling patterns of the SPring-8 storage ring

	Pattern name	Explanation
pattern 1	multi-bunches	(160-bunch train + 43-empty bucket train) × 12 with 50 μA/bunch
pattern 2	203 bunches	203 equally spaced bunches with about 0.5 mA/bunch
pattern 3	1/12 filling + 10 singles	203-bunch train with total of 82 mA + 10 equally spaced isolated bunches with about 1.8 mA/bunch
pattern 4	single bunch	Only one bucket is filled with electrons: 10 mA/bunch

* The harmonic number of the storage ring is 2436; 1/12 × 2436 = 203, etc.

One of the practical countermeasures used to eliminate the filling pattern dependence is to place additional band pass filters (BPFs) whose center frequency is the detection frequency of the circuits, i.e., the RF acceleration frequency, at the inputs of the filter-switch modules. The filters reduce the time domain signal amplitude by restricting unnecessary frequency components while keeping the detection frequency component unchanged. The effect of the amplitude reduction of the BPF is different for the isolated bunches and the bunch train parts. For example, in the hybrid filling patterns such as pattern 3 in Table 1, the amplitudes of the isolated bunches were larger than those of the train part for the signals before the BPF. On the contrary, the amplitude of the train part was larger than those of the isolated bunches for the signals after passing the BPF with 10 MHz bandwidth, because the RF acceleration frequency component contributed significantly in the train part spectrum, whereas components other than the RF acceleration frequency component had a large contribution in the isolated bunch spectrum. To remove the filling pattern dependence, the maximum amplitude must be smaller than the level of the onset of diode conduction after passing the BPF in any possible filling pattern, whether the maximum originates from a train part or from an isolated bunch with a large current.

The elimination of filling pattern dependence for actual beams had to be confirmed before the adoption of the method. For the BPF bandwidth selection, we had several BPF with 10 MHz bandwidth, and the results of some preliminary tests and calculations seemed to be promising. We made additional samples of the 10-MHz-bandwidth BPF and performed measurements to evaluate the effectiveness of the filters by using actual beams in the storage ring. The storage ring was operated in the filling patterns listed in Table 1 for the evaluation. The COD data were compared between the different filling patterns.

From the obtained data, the root-mean-square (rms) values of the differences of COD data between the different filling patterns were calculated. They are listed in Table 2, which shows that the COD differences were all within about 10 μm. The BPF were found to be effective in removing the filling pattern dependence. An example of the differences of the COD data between the different filling patterns is shown in Fig. 13. The BPF were attached to the BPM with serial numbers from 1 through 30. As shown in the figure, the effectiveness of the BPF is evident; the COD data of the BPM with the BPF were reproduced within 10 μm, whereas differences in the COD data of other BPM extended to more than 100 μm.

In accordance with the result, we will produce a sufficient number of BPF to cover the whole storage ring, i.e., more than 1000 pieces, and attach them to

Table 2. Summary of the measurements: rms of COD differences between different filling patterns. All the data are in the unit of μm, δx are in the horizontal and δy are in the vertical direction

Compared pattern	with BPF		without BPF	
	δx_{rms}	δy_{rms}	δx_{rms}	δy_{rms}
(203 bunches) – (multi-bunches)	1.5	4.4	41	51
(1/12filling + 10 singles) – (203 bunches)	6.2	4.1	28	60
(single bunch) – (multi-bunches)	9.0	10.7	2100	3072

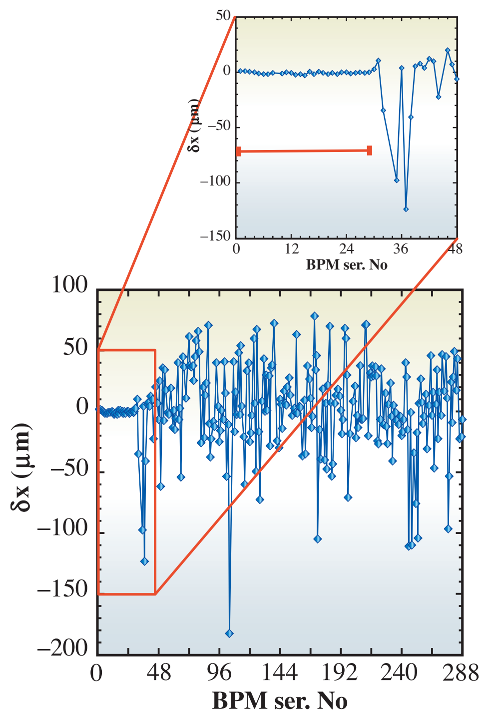

Fig. 13. Example of the COD differences in the horizontal direction between two different filling patterns: the 203 bunches and the multi-bunches. The data of the serial numbers from 1 to 48 are zoomed in the upper plot. The BPF were attached only to the BPM of serial numbers 1 to 30 indicated by the red line in the zoomed plot.

the inputs of filter-switch modules in the summer shutdown of 2008. We expect that, after the summer shutdown, we will be able to operate the storage ring in any filling pattern with a reproducibility of the closed orbit of about 10 μm.

Development of Bunch-by-bunch Feedback

Bunch-by-bunch feedback for filling with high contrast bunch current

The filling of the storage ring with a few high current singlet bunches and trains of low current bunches are requested by users and, for such requests, the ratio of maximum to minimum bunch current is nearly 10. Bunch-by-bunch feedback was installed to suppress transverse beam instabilities. The signal of a bunch from a BPM for feedback, or the gain of feedback, is proportional to the bunch current and the position shift of the bunch and, with the limited dynamic range of the components of feedback and feedback gain, it is difficult for the feedback to handle bunches with such a wide range of bunch current. To overcome this difficulty, we developed a bunch-by-bunch attenuation system, which automatically attenuates the signal from bunches with high bunch current to reduce the contrast of the bunch current (Fig. 14). This attenuator is composed of a fast discriminator that detects the bunch current and produces a gate signal, FPGA, for generating a one-turn delay of the gate signal, and mixers for attenuation driven by the gate signal. Using this attenuator, we could simultaneously store several singlet bunches with bunch current 3 mA/bunch and a bunch train with bunch current 0.6 mA/bunch.

RF direct sampling

For the operation of the bunch-by-bunch feedback since 2007, we have employed the scheme of RF direct sampling for the front-end circuit. The concept of RF direct sampling is shown in Fig. 15. With this scheme, we can eliminate the base-band conversion stage that requires mixers, an LO signal, filters and amplifiers, and simplify the system with fewer tuning points and low cost, as shown in Fig. 16. To perform the RF direct sampling, we chose the Analog Devices AD9433 ADC for the second version of the SPring-8 feedback processor, which was completed in 2005. The analog bandwidth of AD9433 extends up to 750 MHz (full power) and covers the required frequency range for the RF direct sampling, from 250 MHz to 750 MHz, with a bunch rate of 508 MHz.

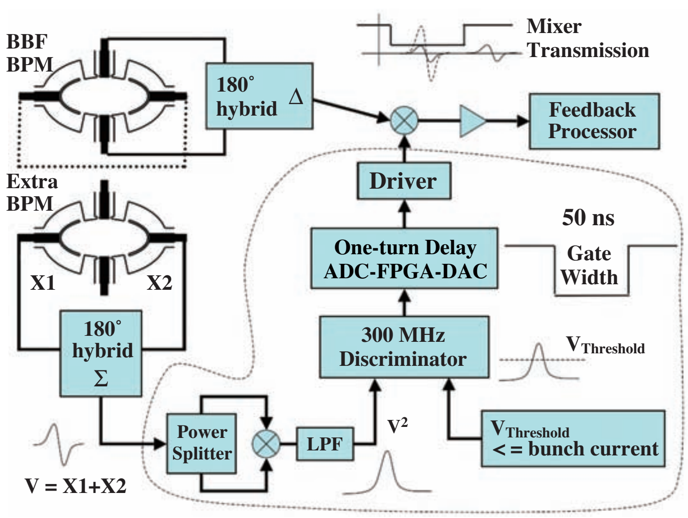

Fig. 14. Block diagram of bunch-current-sensitive automatic attenuation system. The threshold current above which the attenuation is large is controlled by the threshold voltage of the discriminator.

International Collaboration

In 2006, a single-loop two-dimensional transverse bunch-by-bunch feedback unit was successfully installed at SOLEIL storage ring in Paris, France, based on collaboration between JASRI and SOLEIL with the SPring-8 feedback processor. Also in 2006, the digital transverse feedback unit was tested in the Hefei light source at the National Synchrotron Radiation Laboratory (NSRL), University of Science and Technology of China (USTC), Hefei, China, using the feedback unit developed by JASRI during the visit of a researcher from JASRI as part of the collaboration between JASRI and NSRL/USTC.

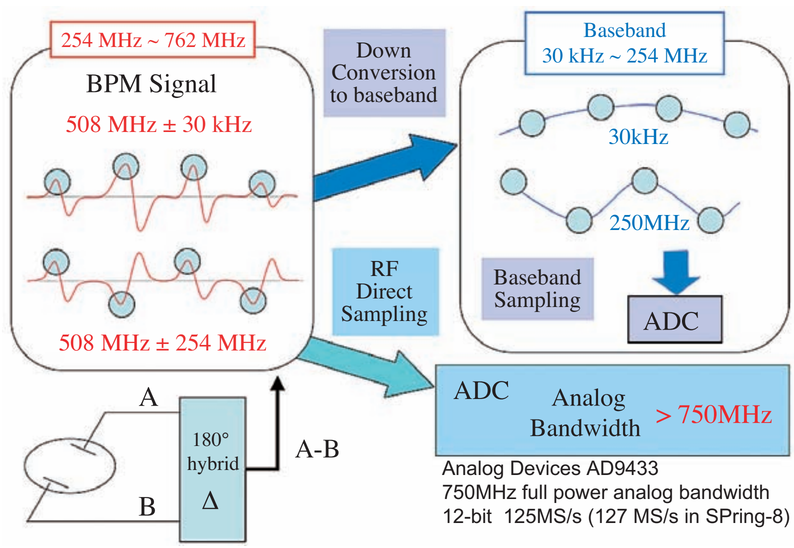

Fig. 15. Concept of RF direct sampling. Base-band conversion and base-band sampling are also shown.

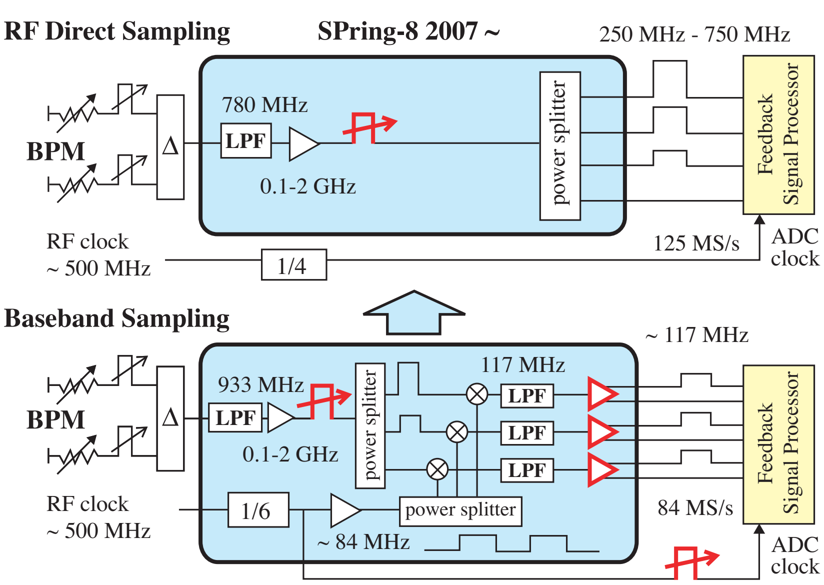

Fig. 16. RF front-end circuit for RF direct sampling in SPring-8. The circuits for base-band conversion and base-band sampling are also shown.

Development of Accelerator Diagnosis Beamlines

At accelerator diagnosis beamline I (BL38B2), a bunch purity monitor has been continuously monitoring the purity of isolated main bunches of several-bunch user operation modes. It is based on the gated photon counting method utilizing two fast Pockels cells as light shutters operating in the visible light region, and can successfully detect parasitic satellite bunches as low as 10^{-9} times the intensity of the main bunches [11]. An example of the evolution of bunch purity during a topping-up user operation measured using the monitor is shown in Fig. 17.

At accelerator diagnosis beamline II (BL05SS), the so-called edge radiation from the bending magnets upstream and downstream of the ID straight section of the beamline can be utilized in optics hutch I. By observing the microwave component of the edge radiation, burst coherent synchrotron radiation originating from instabilities of the intense single bunch beam was surveyed and promising preliminary results were obtained. Figure 18 shows an example of an oscilloscope trace of the output signal obtained from a microwave detector. A significant repeated signal above the noise level at the revolution frequency was observed sporadically for a beam current larger than about 10 mA. By irradiating the X-ray component of the edge radiation to a vacuum gauge head, misreading of a Bayard-Alpert ionization vacuum pressure gauge was studied experimentally [12].

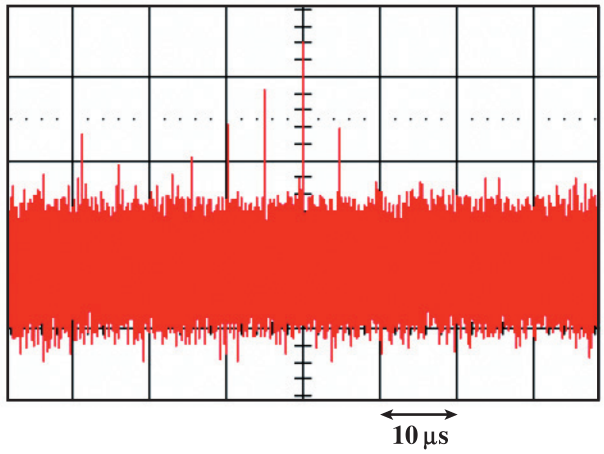

Fig. 18. Example of an oscilloscope trace of output from a microwave detector operating in the 75-110 GHz frequency range. The current of the single bunch was 12 mA. The horizontal scale is 10 μs per division and the revolution period of the bunch is 4.8 μs. A repeated signal above the noise level was observed at the revolution frequency.

The development and installation of the vacuum components of optics hutches I and II of the diagnosis beamline II have been completed (Fig. 19). The first light of the ID was successfully delivered to optics hutch I in May 2007. Optics hutch II has a double crystal monochromator based on the SPring-8

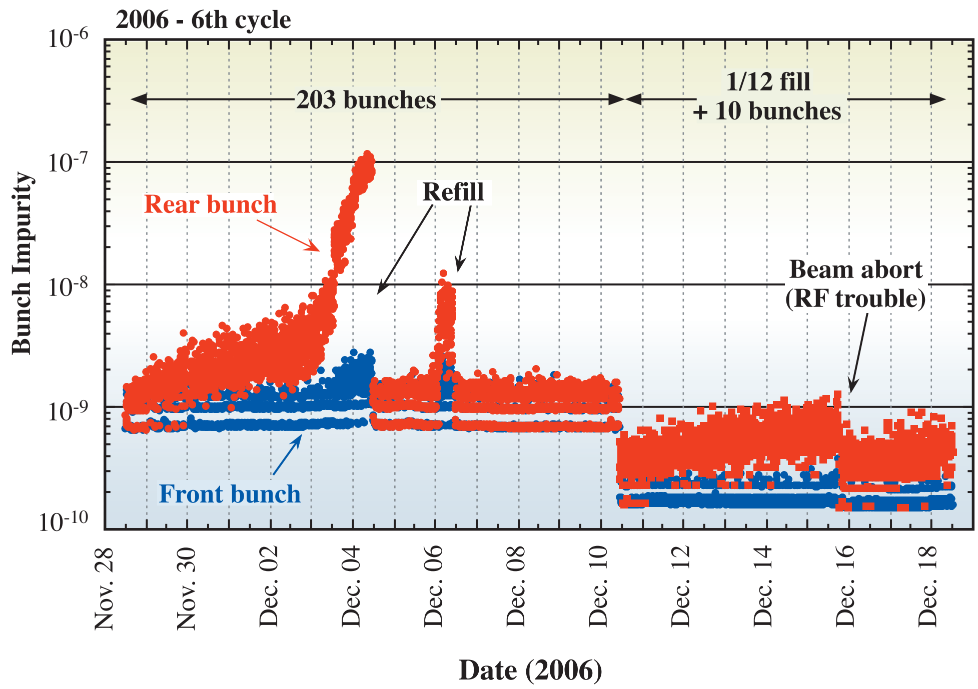

Fig. 17. Example of evolution of bunch purity. The red circles stand for the nearest satellite bunches preceding the main bunches and the blue ones stand for those behind the main bunches. On 4th and 6th December, abortion and refill of the beam were performed, respectively, because of an unacceptable increase of the bunch impurity.

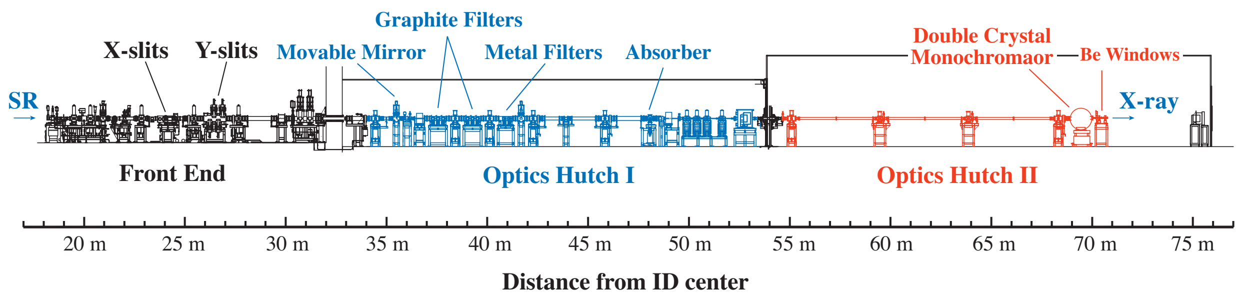

Fig. 19. Schematic layout of accelerator diagnosis beamline II (BL05SS).

standard type. The crystals of the monochromator are cooled by liquid nitrogen. The x- and y-slits used to shape the input X-ray beam of the monochromator have also been installed in the front end. The delivery of the first light of the ID to optics hutch II is planned early in 2008.

Research and Development of 10-T Superconducting Wiggler –Field Measurement–

If a high-field superconducting wiggler (SCW) is installed in the SPring-8 storage ring, it can generate synchrotron radiation with energy of MeV order [13], which is very useful for nuclear astrophysics and other experiments. The SCW consists of one central magnetic pole (main pole) and two side poles. The side poles are excited with opposite polarity to the main pole (see Fig. 20). The maximum field of the main pole is designed to be 10 T in the vertical direction (B_y). The beam orbit deflection in the horizontal plane can be closed within the SCW by adjusting the excitation currents of the main pole and side poles. For orbit stability of less than 1 μm, the field fluctuation must be less than 10^{-6} because the field of the main pole is one order higher than that of the normal dipole magnets. Accurate field measurement is then required. Furthermore, to estimate the total effect on the stored beam, it is necessary to measure not only the main component of the magnetic field B_y but also the minor component in the horizontal direction (B_x) and longitudinal direction (B_s). We then need to measure these components on three-dimensional mesh points to extract the quadrupole and higher multipole fields. For this purpose, we designed a stage for the field measurement of the SCW. Since the beam chamber of the SCW is narrow and long (65 mm in width, 20 mm in height and 1.5 m in length), it is difficult to access the central part of the chamber. We thus

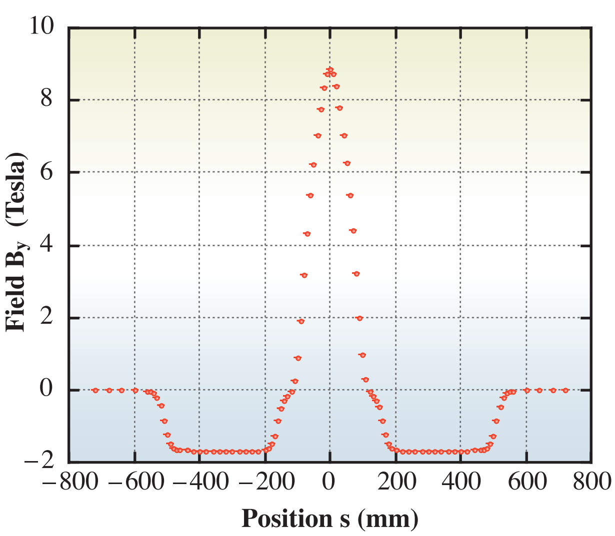

Fig. 20. Longitudinal distribution of the vertical field B_y (measured x = y = 0 mm on the s-axis). The field of the main pole was set to 9 T. The main pole and side poles are located at s = -100 mm ~ +100 mm, s = -500 mm ~ -150 mm and s = +150 mm ~ +500 mm, respectively. Error bars indicate one standard deviation of ten measurements.

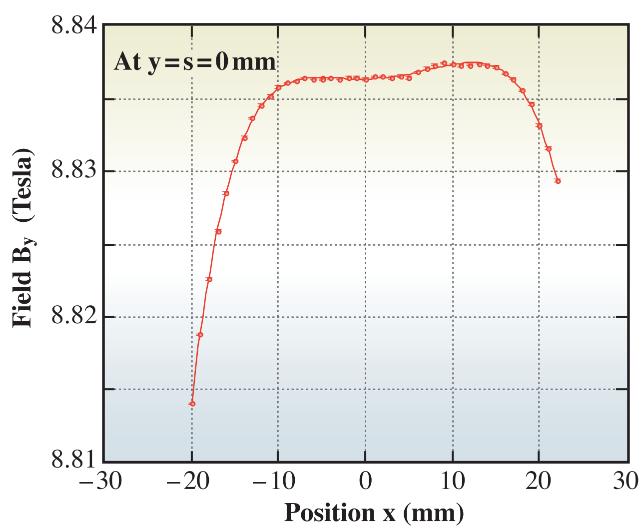

Fig. 21. Horizontal distribution of the vertical field B_y at the position y = s = 0 mm. The field of the main pole was set to 9 T. The solid line indicates the result of least-squares fitting with a polynomial of degree six in x. Error bars indicate one standard deviation of ten measurements.

passed a timing belt through the chamber, on which a three-dimensional hall probe was fixed. The belt forms a loop through the chamber with two gears at both ends. A gear on one side is pulled with a tension of 10^3 N to minimize the bending of the belt. To adjust the longitudinal position of the probe, the belt is rotated by a stepper motor, and to adjust the horizontal and vertical positions, the belt is moved manually using x-y stages set at both ends.

Examples of field measurements are shown in Figs. 20 and 21. In Fig. 20, the longitudinal distribution of the vertical field B_y (measured at x = y = 0 mm on the s-axis) is shown when the peak field was set to 9 T. The horizontal distribution of field B_y at the position y = s = 0 mm is shown in Fig. 21. The longitudinal distribution was consistent with the designed value. To estimate the strengths of the multipole components, the horizontal distribution was fitted by the least-squares method with a polynomial of degree six in x (Fig. 21, solid line). We found that the strengths of the multipole components could not be neglected and were asymmetric to the x-axis and the y-axis. By exciting the SCW several times, we also evaluated the reproducibility of the field and found that it was less than the error of the measurement.

In the future, a three-dimensional field will be measured automatically using automatic x-y stages in the range of x = ±20 mm, y = ±5 mm and s = ±720 mm. The measurement will be carried out with a 1 T step of the peak field. The field measurement data will be used for designing dipole, quadrupole, sextupole and, if necessary, higher multipole corrector magnets for compensating the SCW error field to suppress the effect on the stored beam.

Research and Development of Femto-second Pulse X-ray Generation

The principle of femtosecond pulse X-ray (FSX) generation studied at SPring-8 is as follows: RF deflectors installed in the storage ring vertically kick the head and tail of a stored bunch in opposite directions. Thus, the bunch is tilted and emits a tilted photon bunch in the undulator downstream. A slit further downstream slices the photon bunch to form a short pulse light. The plan to achieve FSX generator under consideration and its design parameters are detailed in a previous report [14].

In this report we presents performance achievable by the short X-ray generator. In the following discussion, we assume that all electron and photon bunches have Gaussian distributions. Note that the symbol "σ" meaning pulse width corresponds to a standard deviation of a Gaussian distribution.

Photon flux density and extraction efficiency

We have studied two types of undulators operating at SPring-8, the minipole undulator [15] and the standard-type undulator. The parameters of the undulators designed for FSX generation are listed in Table 3.

Table 3. Parameters of undulators designed for FSX generation

Type of Undulator	Period Length	Gap	K Value	Total Period
Mini-Pole Type	10 mm	5 mm	0.92	101
Standard Type	32 mm	10 mm	2	140

The above minipole undulator has the advantage of a smaller diffraction-limited spot size than the standard type. The photon flux density from the minipole undulator at a stored current of 100 mA is shown in Fig. 22. The photon energy and flux density of the first peak are 10.7 keV and 8.48 × 10^{17} photons/(sec·mrad²·0.1% BW·100 mA) at an electron beam energy of 4GeV, and 42.5keV and 8.48 × 10^{17} at 8 GeV, respectively. The brilliance of the first peak corresponds to 5.34 × 10^{20} Photons/ (sec·mm²·mrad²·0.1% BW·100 mA) for 4 GeV and 1.62 × 10^{20} for 8 GeV.

Although the operating energy of the SPring-8 storage ring is 8 GeV, low energy operation at 4 GeV is being considered to improve the beam emittance. The dashed lines in Fig. 22 show the first peak shift as the K value approaches zero.

The extraction efficiency η, defined as the ratio of the X-ray flux sliced by the slit to the total flux emitted

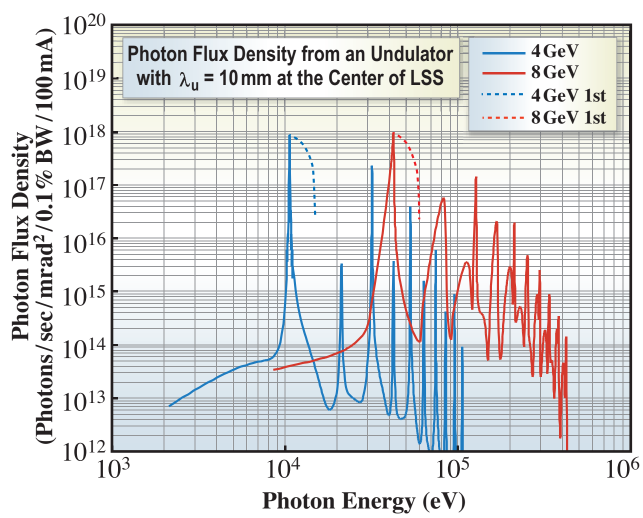

Fig. 22. Spectrum of photon flux density from the minipole undulator suitable for short-pulse generation. The intensities correspond to 100% extraction efficiency.

from the entire bunch, is approximated by

$$\eta \cong \frac{2W}{\sqrt{2\pi}\sigma_t c \tan\theta_{tilt}} \ , \qquad (1)$$

where $2W$ is the full width of the slit, σ_t is the longitudinal bunch length in time and $\tan\theta_{tilt}$ is the bunch tilt. Figure 22 corresponds to the case of η = 1, or 100% efficiency.

Pulse width

The extracted X-ray pulse width σ_p is described by

$$\sigma_p^2 \cong \sigma_{p0}^2 + \left(\frac{W}{\sqrt{6}c\tan\theta_{tilt}}\right)^2 , \qquad (2)$$

where σ_{p0} is the minimum X-ray pulse width attained by the FSX generator, given by

$$\sigma_{p0} = \sqrt{\sigma_y^2 + \sigma_r^2} \Big/ c\tan\theta_{tilt} \ , \qquad (3)$$

where σ_y is the vertical bunch size given by the emittance and β function, and σ_r is the diffraction limited spot size. This formula implies that we require smaller σ_y and σ_r and larger $\tan\theta_{tilt}$ to realize a shorter pulse width, where σ_y is dominated by the accelerator parameters and σ_r is mainly dominated by the insertion device parameters.

RF deflector – the crab cavity –

The bunch tilt $\tan\theta_{tilt}$ is given by

$$c\tan\theta_{tilt} = \frac{2\pi f_{def} L_{drift} eV_{\perp}}{E_{electron}} \ , \qquad (4)$$

where f_{def} and $V_{\perp}$ are the deflecting frequency and the voltage of the RF deflector, respectively. L_{drift} is the length of the drift space between the RF deflectors and $E_{electron}$ is the electron beam energy. In our design, L_{drift} is 7 m. From Formulae (2), (3) and (4) we find that a larger deflecting voltage is required to obtain a shorter X-ray pulse.

We employed a superconducting crab cavity developed at KEK [16] as a deflector, which has achieved a maximum deflecting voltage 2.7 MV for CW operation at 4.2 K, and its resonant frequency of 508.887 MHz is almost as same as that of 508.58 MHz of the SPring-8 storage ring. The crab cavity is operated in the TM_{110} mode and the bunch is kicked vertically by its horizontal magnetic field. The magnetic path integral in the cavity is converted into the effective deflecting voltage. In this paper we conservatively assumed the old value of 1.67 MV as the deflecting voltage of the cavities, and consequently obtained a bunch tilt $c\tan\theta_{tilt}$ of 13.3 μm/psec at 4 GeV (and 6.67 μm/psec at 8 GeV) for the 7 m drift space.

Performance of FSX – pulse width and extraction efficiency –

We evaluated the performance of the FSX sliced from the first peak X-ray. From Formulae (1) to (4) the relation between the sliced light pulse width and the extraction efficiency can be obtained for the minipole undulator (λ_u = 10 mm) and the standard-type undulator (λ_u = 32 mm) as shown in Fig. 23. In this calculation the diffraction effect was considered and the beam emittance was assumed to be $\varepsilon_y = 0.75 \times 10^{-12}$ m·rad at 4 GeV and $\varepsilon_y = 3 \times 10^{-12}$ m·rad at 8 GeV. If we assume the extraction efficiency to be 1% at 4 GeV operation, we can obtain a pulse width of 600 fs in two standard deviations. As the pulse width approaches the attainable minimum σ_{p0}, the extraction efficiency falls drastically.

According to Fig. 23, the minimum light pulse widths are determined by the parameters of the undulators in the case of 4 GeV operation, whereas they are almost unique in the case of 8 GeV operation. That is, the diffraction limited spot size is dominant at 4 GeV, as indicated by Formula (3), and therefore, it is effective to introduce the minipole undulator. On the other hand, the standard-type undulator operates satisfactorily at 8 GeV, as the vertical beam size given by the emittance is dominant at this beam energy.

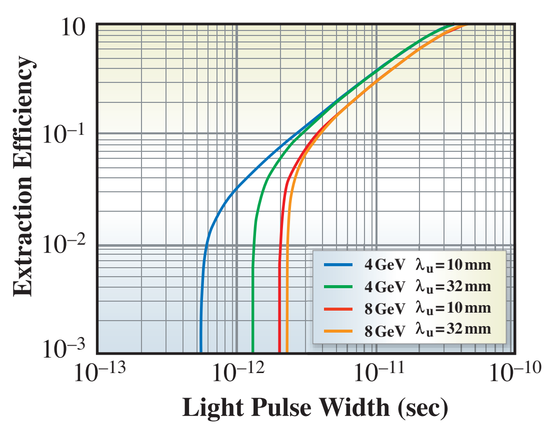

Fig. 23. Relation between the pulse width and the extraction efficiency. The pulse width is the value representing two standard deviations.